# Unlocking Sustainable Nitrate Reduction: Earth-Abundant Bimetallic Electrodes Under Galvanostatic Evaluation

Gabriel Antonio Cerrón-Calle, Andrea Maya, Diana Leon, Manuel Roldan, Ana S Fajardo, Carlos M Sánchez-Sánchez, Sergi Garcia-Segura

# Unlocking Sustainable Nitrate Reduction: Earth-Abundant Bimetallic Electrodes Under Galvanostatic Evaluation

Gabriel Antonio Cerrón-Calle[a], Andrea Maya[a], Diana Leon[a], Manuel Roldan[b], Ana S. Fajardo[a,c,d,e], Carlos M. Sánchez-Sánchez[c], Sergi Garcia-Segura[a,*]

[a]Nanosystems Engineering Research Center for Nanotechnology-Enabled Water Treatment, School of Sustainable Engineering and the Built Environment, Arizona State University, Tempe, AZ 85287-3005, USA

[b]Eyring Materials Center, Arizona State University, Arizona 85287, USA

[c]Sorbonne Université, CNRS, Laboratoire Interfaces et Systèmes Electrochimiques (LISE), 4 place Jussieu, F-75005, Paris, France

[d]Polytechnic Institute of Coimbra, Applied Research Institute, Rua Da Misericórdia, Lagar Dos Cortiços – S. Martinho Do Bispo, 3045-093 Coimbra, Portugal

[e]Research Centre for Natural Resources, Environment and Society (CERNAS), Polytechnic Institute of Coimbra, 3045-601 Coimbra, Portugal

*The article submitted to be published in*

*Electrochimica Acta*



Corresponding author:

*e-mail: sergio.garcia.segura@asu.edu (Dr. Sergi Garcia-Segura)

**Abstract**

The electrochemical reduction of nitrate (ERN) has emerged as a green alternative to alleviate the $NH_3$ production via the Haber-Bosch process. Harnessing earth-abundant materials for electrocatalysts is a logical strategy, minimizing dependence on the cost-prohibitive platinum group elements. While

previous research has delved into the preparation and evaluation of electrodes for $NH_3$ generation, much of it has been mainly focused on potentiostatic conditions and mechanisms elucidation, overlooking real-world scenarios precluding the advancement towards technology implementation. This study addresses this gap by screening the performance of earth-abundant bimetallic electrodes, leveraging Cu foam as a substrate and modifying it with $Cu_2O$, $Ni(OH)_2$, $SnO_2$, and $Co(OH)_x$ through electrodeposition. A comprehensive characterization encompassing morphological, structural, and electrochemical analysis was performed on the novel bimetallic surfaces. Electrolysis experiments targeting 30 mg $L^{-1}$ $NO_3^-$-N were conducted under galvanostatic conditions (2.5, 5, 10, 20, and 40 mA $cm^{-2}$), revealing the following trend in $NH_3$ yield (mmol $NH_3$ $g_{cat}^{-1}$ $h^{-1}$): $Cu/Co(OH)_x$ > $Cu/Cu_2O$ > Cu foam > $Cu/SnO_2$ > $Cu/Ni(OH)_2$. Engineering figures of merit required for techno-economic analysis, such as Faradic efficiency, electrical energy per order, kinetic constants, and $NH_3$ generation efficiency, were estimated for each configuration. This study not only sheds light on the operational conditions of ERN but also offers a roadmap toward sustainable and economically viable $NH_3$ production.

**Keywords:** Ammonia generation, copper oxide, nickel hydroxide, tin oxide, cobalt hydroxide, direct current

## 1. Introduction

The world's population is on track to reach 8.5 billion by 2030 [1]. Ammonia-based fertilizers have been vital in facilitating this growth by significantly enhancing food production over the past century, supporting approximately 50% of the global population [2]. As a result, ammonia ($NH_3$) has emerged as one of the pivotal chemicals in the food industry [3,4]. The Haber-Bosch process, responsible for producing over 450 million metric tons of $NH_3$ in 2022, combines nitrogen ($N_2$) and hydrogen ($H_2$) under high temperatures and pressures using an iron (Fe) catalyst [5]. However, despite its critical role in global $NH_3$ production, this process has a substantial carbon footprint, contributing to around 2% of global $CO_2$ emissions [6,7]. Given that Haber-Bosch dominates large-scale $NH_3$ output, producing approximately 1200 metric tons per day, there is a growing need to develop sustainable alternatives for $NH_3$ production, particularly tailored to medium- and small-scale operations [3,8,9].

Nitrate ion ($NO_3^-$) represents an untapped N-source small molecule with high solubility in water and a lower energy barrier (245 kJ $mol^{-1}$) compared to $N_2$ [10–12]. Nevertheless, the electrochemical reduction of nitrate (ERN) involves a complex multi-step 8-electron reaction to produce $NH_3$ [13–15], but other contaminant products are also formed such as nitrite ($NO_2^-$) in solution and different N-gas species (i,e., $N_2$, NO, $NO_2$, $N_2O$). Thus, modifying the electrode chemical composition [16], as well as its interface [17], impact on the ERN catalytic performance and selectivity. Hence, the strategic design of catalysts becomes essential in identifying materials with high selectivity towards $NH_3$ and fast kinetics.

Both experimental and theoretical studies have identified platinum group materials (PGMs) like iridium (Ir), ruthenium (Ru), and platinum (Pt) as promising candidates for achieving high $NH_3$ yield [18–25]. However, the prohibitive cost associated with these materials limits the feasibility of the process [26,27]. As a result, there is a pressing need to shift research efforts towards sustainable and environmentally compatible earth-abundant materials, including copper (Cu), cobalt (Co), nickel (Ni), tin (Sn), iron (Fe), and manganese (Mn). Exploring various electrode compositions such as alloys, oxides, hydroxides, bimetallic, and multimetallic configurations holds significant promise in ERN [28–34]. Among these, Cu-based electrodes appeared as potentially viable alternatives for $NH_3$ production from ERN. The negative energy adsorption of $NO_3^-$ on Cu surfaces promotes efficient electron transfer at the electrode surface [35,36]. However, it is essential to note that Cu surfaces also exhibit high adsorption of $NO_2^-$, which may lead to $NO_2^-$ accumulation because Cu-based electrodes exhibit much higher activity for $NO_3^-$ than for $NO_2^-$ reduction. In particular, introducing Ni sites may be an alternative to boost electron transfer for $NO_2^-$ reduction and provide sites for binding atomic hydrogen adsorption *H necessary for $NH_3$ production [37,38]. Studies using Sn in conjunction with Pt and Pd demonstrate that Sn sites exhibit high $NO_3^-$ conversion to $NO_2^-$ [39–41]. Moreover, adding Co sites have shown experimental and theoretical capabilities in facilitating hydrogenation steps of $NO_3^-$ reduction intermediates [42–44]. Therefore, the use of bimetallic or multimetallic Cu-based electrodes could transform the inherent disadvantage of pristine Cu into an advantage by enhancing $NH_3$ production. Furthermore, these elements are affordable, with prices ranging from 3.8 to 12.8 \$ $lb^{-1}$ compared with Pd, which costs more than 14 500 \$ $lb^{-1}$ according to market prices [45].

When evaluating electrodes for ERN and other small molecules, assessments typically occur under potentiostatic conditions [10,46,47]. However, translating these findings to real-world field applications can prove challenging due to the complexities introduced by the three-electrode configuration. Potentiostatic conditions in large-scale systems are not feasible. Three electrode systems require a reference electrode, which proves challenging to implement when using large electrodes due to different current distributions on larger electrode dimensions. These challenges are aggravated especially in complex water matrices as those detrimentally affect the reference electrodes. Overall, this translates in the need for close technician attendance and therefore intermittent operation [48]. In contrast, galvanostatic conditions employing a two-electrode configuration offer a more practical evaluation of materials for real-world field applications. For example, industries focused on electrocoagulation, electrodesalination, electrooxidation, electrolyzers, cooling tower systems, electrowinning, electrochlorination systems, among others, are well-advanced electrochemical technologies working under galvanostatic conditions. Despite this advantage, galvanostatic studies are scarcely reported in literature for ERN. Fundamental potentiostatic experiments often exhibit higher Faradaic efficiencies than galvanostatic ones due to the avoidance of parasitic reactions in ultrapure waters, but these values may not directly inform large scale designs, despite their significance in advancing fundamental science. Bridging the gap between fundamental electrochemical studies and real-world applications necessitates reporting electrode performance under more representative operational conditions for larger engineered systems.

This study addresses this need through the galvanostatic evaluation of bimetallic electrodes modified on tridimensional (3D) Cu foam with Cu, Co, Sn, and Ni composites via an electrodeposition method. The bimetallic surfaces were morphologically, structurally, and electrochemically characterized. Intrinsic catalytic activity for ERN was examined under potentiostatic conditions and normalized by the electrochemical surface area (ECSA). Time-course N-species mass balances were conducted at a fixed current density of 20 mA $cm^{-2}$, identifying electrode composition, which exhibit high $NH_3$ yield. Moreover, the electrochemical reduction of $NO_2^-$ was studied here to identify Cu-modified electrodes with high kinetics, reducing $NO_2^-$ generated by Cu foam. Additionally, engineering figures of merit at different current densities were calculated to provide $NH_3$ yield rate, Faradaic efficiency, and electrical energy per order, essential parameters for subsequent techno-economic analyses.



## 2. Materials and methods

### *2.1 Chemicals and materials*

All chemicals used were acquired from Sigma-Aldrich at analytical purity grade or higher and used without further purification. Earth-abundant nanocomposites were synthesized using anhydrous coppers sulfate ($CuSO_4$ ≥ 99.0%), nickel sulfate ($NiSO_4{\cdot}6H_2O$ ≥ 99.0%), tin chloride ($SnCl_2$ ≥ 99.0%), and cobalt sulfate hexahydrate ($CoSO_4{\cdot}6H_2O$ ≥ 99.0%) as metal precursors. Boric acid ($H_3BO_3$ ≥ 99.5%), sulfuric acid ($H_2SO_4$ ≥98%), and sodium sulfate ($Na_2SO_4$ ≥ 99.0%) served as additives and electrolyte supports in specific electrochemical bath compositions. Model solutions containing inorganic N-species

such as sodium nitrate ($NaNO_3$), sodium nitrite ($NaNO_2$), or ammonium sulfate ($(NH_4)_2SO_4$) were prepared with reagents of analytical grade (≥ 99.0%). All solutions were prepared using ultrapure water with resistivity >18.2 MΩ cm (Elga Water) at 25 °C. Copper foam acquired from Futt (99.99% purity, 110 pores per inch, 2 mm thick) was used as the substrate of three-dimensional nano-enabled electrodes with a geometrical area of 1.5 x 1.5 $cm^2$. Acetone ($(CH_3)_2CO$, ≥ 99.5%) and hydrochloric acid (HCl, ≥ 37.0%) were employed for copper foam pretreatment.

*2.2 Synthesis of the nano-enabled electrodes*

The pretreatment of Cu foam before electrodeposition involved a series of steps: firstly, immersion in an ultrasonic bath containing acetone for 15 min to remove organic compounds, followed by a 5 min soak in 1.0 mol $L^{-1}$ HCl solution to remove surface oxides. Finally, electrodes were rinsed thoroughly with ultrapure water and air-dried at room temperature. For the modification of Cu foam, chronoamperometric electrodeposition was used, with potential controlled by a potentiostat (Metrohm, PGSTAT302N, USA). This process took place in an open three-electrode configuration, using Ag/AgCl (3.2 mol $L^{-1}$ KCl) as the reference electrode, platinum plate as counter-electrode, and Cu foam (1.5 cm x 1.5 cm) as the working electrode. Optimal electrodeposition conditions for each bimetallic configuration are summarized in Figure 1. All experimental conditions for bimetallic electrode synthesis were defined based on the reduction potential for metal depositions according to their corresponding cyclic voltammetry, and the achieved $NO_3^-$ conversion for electrode material prepared at different electrodeposition times (see Figure S1). Following deposition, electrodes were air-dried at room temperature, and their masses were recorded for further calculations.

*2.3 Characterization of the three-dimensional electrodes*

The morphological distribution of nanocomposites was explored using a field emission scanning electron microscope (FE-SEM, Zeiss Auriga) operating at 5.0 keV with a working distance of 5 mm. Structural and elemental characterization was performed using a scanning transmission electron microscope JEOL JEM-ARM-200F operated at 200 kV and an Oxford Instruments Aztec energy-dispersive X-ray spectrometer (STEM-EDS). Samples for STEM-EDS of earth-abundant composites were obtained by sonication of bulk electrodes on ethanol and drop casting the obtained solution on carbon film-supported gold grids. To study the oxidation state of elements, X-ray photoelectron spectroscopy (XPS, Kratos Axis Supra+) was employed. The XPS system contained a dual monochromatic Al/Ag source with high energy resolution (Al $K_\alpha$ = 1486.6 eV and Ag $L_\alpha$ = 2984.2 eV), providing a line width 0.48 eV on Ag $3d_{5/2}$ and 0.408 eV on Si $2p_{3/2}$.

All electrochemical characterization by cyclic voltammetry and linear sweep voltammetry was performed using a potentiostat (Metrohm, PGSTAT302N, USA) in a typical three-electrode cell configuration. The setup comprised a Pt plate as the counter-electrode, Ag/AgCl (3.2 mol $L^{-1}$ KCl) as the reference electrode, and Cu foam modified with earth-abundant nanocomposites as the working electrode. Before electrochemical measurements, solutions were purged with Ar.

*2.4 Electrochemical reduction of nitrate and nitrite*

The electrochemical reduction of nitrogen species was conducted in an open-air batch glass reactor under magnetic stirring at 500 rpm to ensure mass transfer at 25 °C. The non-deaerated solution to be treated (100 mL) contained either 30 mg $NO_3^-$-N $L^{-1}$ or 30 mg $NO_2^-$-N $L^{-1}$ in 12.5 mmol $L^{-1}$ $Na_2SO_4$. The initial pH and conductivity values were 6.35 ± 0.2 and 3.15 ± 0.05 mS $cm^{-1}$ for $NO_3^-$ and 5.90 ± 0.2 and 3.20 ± 0.05 mS $cm^{-1}$ for $NO_2^-$, respectively. Electrolysis were performed in a two-electrode system under galvanostatic conditions, using a TENMA 72-2720 DC power supply. Cu foam and nano-enabled electrodes served as cathodes, while a commercial Ti/$IrO_2$ (DeNora – USA) acted as the anode. The applied current intensity was determined based on the geometrical area of the electrodes (4.5 $cm^2$) and areal density (0.32 g $cm^{-2}$) provided by the manufacturer. The interelectrode distance between the anode and cathode was maintained at 1.0 cm. Samples were withdrawn periodically and analyzed for N-species concentration, pH, and conductivity. All experiments were performed in triplicate, with sample standard deviations consistently below 5% for all trials.

*2.5 Analytical techniques, equipment, and system performance evaluation*

The pH and conductivity values were measured using Thermo Scientific Orion Star A221 and Orion Star A322 meters, respectively. The concentration of nitrogen species, such as nitrate (mg $L^{-1}$ $NO_3^-$-N), nitrite (mg $L^{-1}$ $NO_2^-$-N), and ammonia (mg $L^{-1}$ $NH_3$-N), over time was quantified using colorimetric methods using TNT 835 (λ = 345 nm), TNT 839 (λ = 515 nm) and TNT 830 (λ = 694 nm) HACH kits with a HACH DR6000 UV-vis spectrophotometer. Concentrations of N-volatile species ($N_2$, NO, $NO_2$, or $N_2O$) were obtained by the difference between the initial N-content and the N-content at a given time of aqueous species. Nitrate conversion was determined using Eq. (1)

$$Nitrate\ conversion\ (\%) = \frac{C_{X,i} - C_{X,t}}{C_{X,i}} \times 100 \quad (1)$$

where $C_{X,i}$ and $C_{X,t}$ are the initial and final nitrate concentrations.

The ammonia yield was calculated using Eq. (2)

$$NH_3\ yield = \frac{C_{NH_3}\, V}{m_{electrocat}\, t} \quad (2)$$

where $C_{NH_3}$ is $NH_3$ concentration in mmol $L^{-1}$, V is the volume of the solution to be treated in L, $m_{electrocat}$ is mass of the electrocatalyst in g, and $t$ is time in h.

The selectivity towards $NH_3$ ($S_{NH_3}$) was determined following Eq. (3), and the $NH_3$ generation efficiency can be estimated by Eq. (4). Selectivity represents the percentage of $NH_3$ electrogenerated from the reduced $NO_3^-$, whereas $NH_3$ generation efficiency indicates the amount of electrogenerated $NH_3$ related to the theoretical maximum achievable if all the initial $NO_3^-$ concentration in solution was reduced solely to $NH_3$. $NH_3$ generation efficiency serves as an engineering metric for efficiently recovering added-value resources, encompassing both selectivity and conversion attained during treatment time.

$$S_{NH_3}(\%) = \frac{C_{NH_{3,exp}}}{C_{nitrate,i} - C_{nitrate,t}} \times 100 \quad (3)$$

$$NH_3\ generation\ efficiency\ (\%) = \frac{C_{NH_{3,exp}}}{C_{NH_{3,theo}}} \times 100 \quad (4)$$

where $C_{NH_{3,exp}}$ is the $NH_3$ concentration experimentally obtained in mg $NH_3$-N $L^{-1}$ for $S_{NH_3}$ and mmol $L^{-1}$ for $NH_3$ generation efficiency, $C_{nitrate,i}$ and $C_{nitrate,t}$ corresponds $NO_3^-$ concentration in mg $NO_3^-$-N $L^{-1}$ before and after treatment, respectively. The $C_{NH_{3,theo}}$ is the theoretical $NH_3$ concentration in mmol $L^{-1}$ if the entire initial amount of $NO_3^-$ is converted to $NH_3$.

Regarding the engineering figures of merit, the Faradaic efficiency (*FE*) and the electrical energy per order (*EE/O*) were determined by Eq. (5) and Eq. (6), respectively. The *FE* evaluates system performance by comparing the actual number of electrons consumed in an electrochemical reaction to the theoretical expected conversion ruled by Faraday's law. At the same time, *EE/O* represents the electric energy required to reduce the concentration of $NO_3^-$ concentration by one order of magnitude in a unit volume during batch operation mode.

$$FE(\%) = \frac{n\ F\ N_i}{3600\ I\ t} \times 100 \quad (5)$$

$$EE/O\ (kWh\ m^{-3} order^{-1}) = \frac{E_{cell} I t}{V_s log(C_0/C_t)} \quad (6)$$

where *n* is the number of electrons required per mol of ammonia in mol, *F* is the Faraday constant (96 487 C $mol^{-1}$), $N_i$ is the mol of $NH_3$ generated during the electrolysis, *I* is the applied current intensity in A, *t* is the electrolysis time in h, and *3600* is a unit conversion factor (3600 s $h^{-1}$). $E_{cell}$ represents the average of the cell potential in V, $V_s$ is the volume of the solution in L, and $C_0$ and $C_t$ are the initial and final $NO_3^-$concentrations.

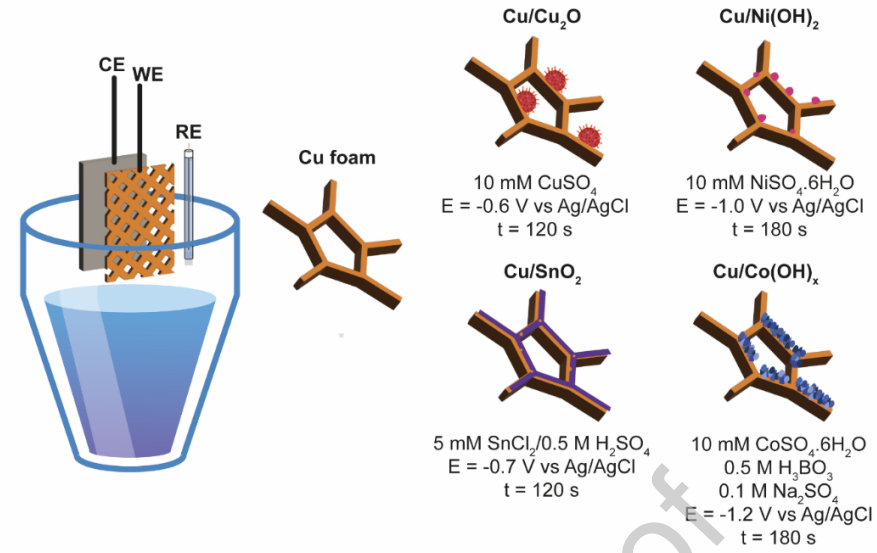


**Figure 1.** Summary schemes of experimental conditions containing electrochemical bath concentrations, applied potential, and optimal time to prepare different bimetallic electrodes in a three-electrode configuration cell.

## 3. Results and discussion

### *3.1. Electrodeposition generates electrocatalytic earth-abundant bimetallic surfaces*

The electrochemical modification of Cu foam with various earth-abundant compounds was morphologically characterized using FE-SEM images. Figures 2a and 2b depict the configuration of Cu foam, featuring an average pore size of 167.8 ± 28.6 µm and a pore pillar width of 55.7 ± 4.7 µm, resulting in a calculated pore per inch (PPI) of approximately 115.0 ± 14. At higher magnification (Figure 2c), the smooth Cu foam surface resembles fish scales, with some craters but devoid of particles. Upon modification with $Cu_2O$ nanocomposites (Figure 2d), the Cu foam surface exhibits nano-urchin particles with a wide size range around 138.2 ± 39.6 nm. Electrodeposition of $Ni(OH)_2$ yields nanosphere composites on the foam surface (Figure 2e), characterized by an average size of 119.7 ± 21.2 nm. Following the electrodeposition of $SnO_2$ nanoparticles, the surface displays high area coverage, forming a thin film with particle sizes averaging 52.7 ± 7.0 nm (Figure 2f). Finally, the electrodeposition of $Co(OH)_x$ nanoflakes results in an average particle size of 98.7 ± 28.1 nm (Figure 2g). These findings underscore the diverse shapes generated from the electrodeposition of different compounds and highlight the generation of bimetallic surfaces, exposing Cu foam and metal composite nanoparticles that alter the overall morphology of the system.

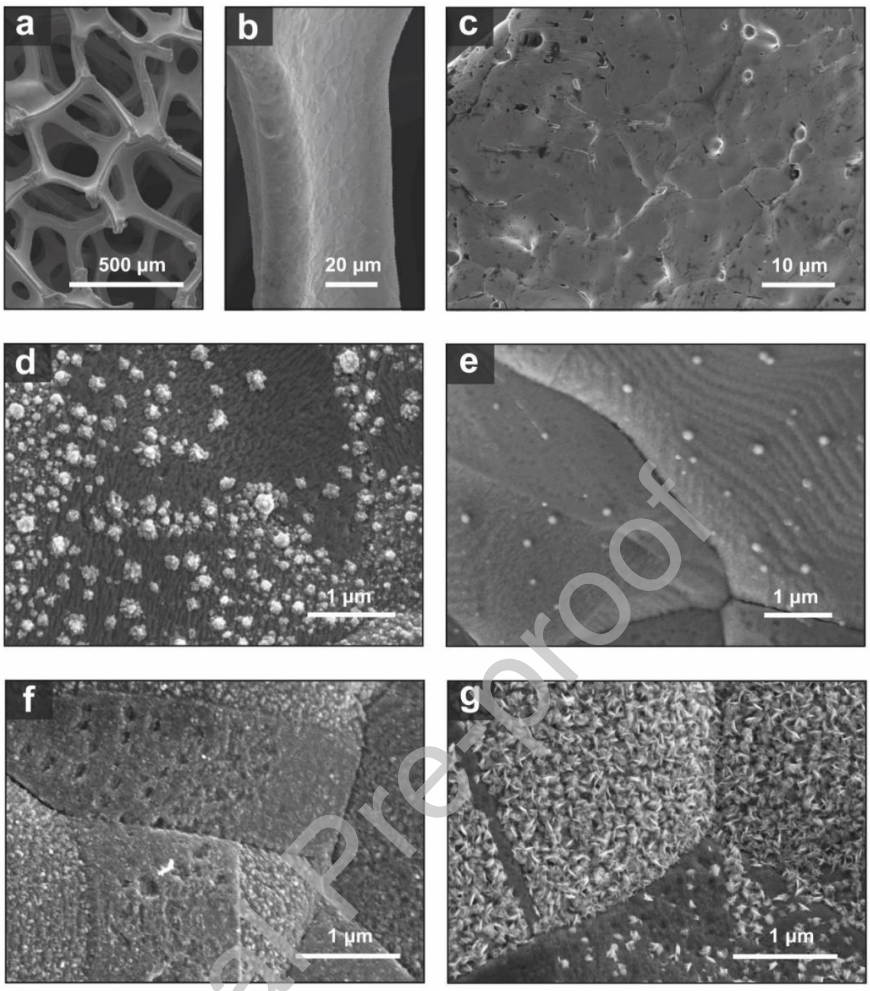


**Figure 2.** SEM images of Cu foam (a), (b), and (c) at different magnifications, (d) $Cu/Cu_2O$, (e) $Cu/Ni(OH)_2$, (f) $Cu/SnO_2$, and (g) $Cu/Co(OH)_x$.

The electrodeposition modification was through elemental mapping via energy dispersive spectroscopy (EDS-mapping), scanning transmission electron microscope (STEM) bright-field (BF) images, and chemical identification by X-ray photoelectron spectroscopy (XPS). Initially, characterization of the Cu foam provided a pristine substrate for comparison with various nano-enabled compounds generated during the electrodeposition process. Figure S2 displays the EDS mapping, predominantly revealing the presence of Cu and O on the surface, where the presence of oxygen can be attributed to inevitable oxide formation under atmospheric conditions after the cleaning treatment. Crystallographic structure, determined using interplanar distance obtained from BF-STEM images, identifies the plane (111) in CuO with an interplanar distance of 0.21 nm for bare Cu foam [49]. High-resolution Cu 2p XPS spectra demonstrate the presence of $Cu^{2+}$ and $Cu^{+1}/Cu^0$ at 934.6 and 932.2 eV, respectively, with a shake-up satellite confirming CuO in the pristine foam [50,51].

In Figure 3a, EDS mapping after modification with $Cu_2O$ indicates the uniform distribution of Cu and O elements on the particles obtained after sonication treatment. Crystal structure identification by BF-STEM image reveals an interplanar distance of 0.30 nm corresponding to the plane (110) present in the $Cu_2O$ structure [52,53]. Additionally, the high-resolution Cu 2p XPS spectra demonstrate a higher intensity for $Cu^{+1}/Cu^0$ than $Cu^{2+}$, supporting the plane obtained by BF-STEM. Figure 3b shows the EDS mapping of the bimetallic surface Cu foam and $Ni(OH)_2$, evidencing the coexistence of Cu and Ni elements in the particle. BF-STEM images identify an interplanar distance of 0.27 nm corresponding to the plane (100) present in the $Ni(OH)_2$ structure [54,55]. Moreover, the high-resolution XPS spectra for Ni 2p demonstrate the coexistence of $Ni^{2+}$ and $Ni^{3+}$ at 853.2 and 854.6 eV, respectively. Figure 3c presents the EDS mapping for $Cu/SnO_2$, evidencing the uniform distribution of Cu and Sn elements on the particle, confirming the successful generation of the bimetallic electrode. The interplanar distance determined by BF-STEM identifies an interplanar distance of 0.25 nm corresponding to the plane (101) in the $SnO_2$ structure [56,57]. Furthermore, XPS spectra for Sn 3d demonstrate the predominant $Sn^{4+}$ compared to $Sn^0$ at 486.6 and 485.0 eV, respectively [58]. Finally, the $Cu/Co(OH)_x$ EDS mapping demonstrates the coexistence of Cu and Co elements on the electrode surface. The BF-STEM image determines an interplanar distance of 0.27 nm corresponding to the plane (010) in the $Co(OH)_2$ structure [59]. Nevertheless, the Co 2p XPS spectra suggests the coexistence of $Co^{2+}$ and $Co^{3+}$ at 779.6 and 782.1 eV, respectively [60,61]. According to these results, the bimetallic electrodes obtained represent an intricate surface with different composites of the elements generating different sites for adsorption and electron transfer processes. Therefore, under practical conditions, the materials prepared are designated as Cu foam, $Cu/Cu_2O$, $Cu/Ni(OH)_2$, $Cu/SnO_2$, and $Cu/Co(OH)_x$.

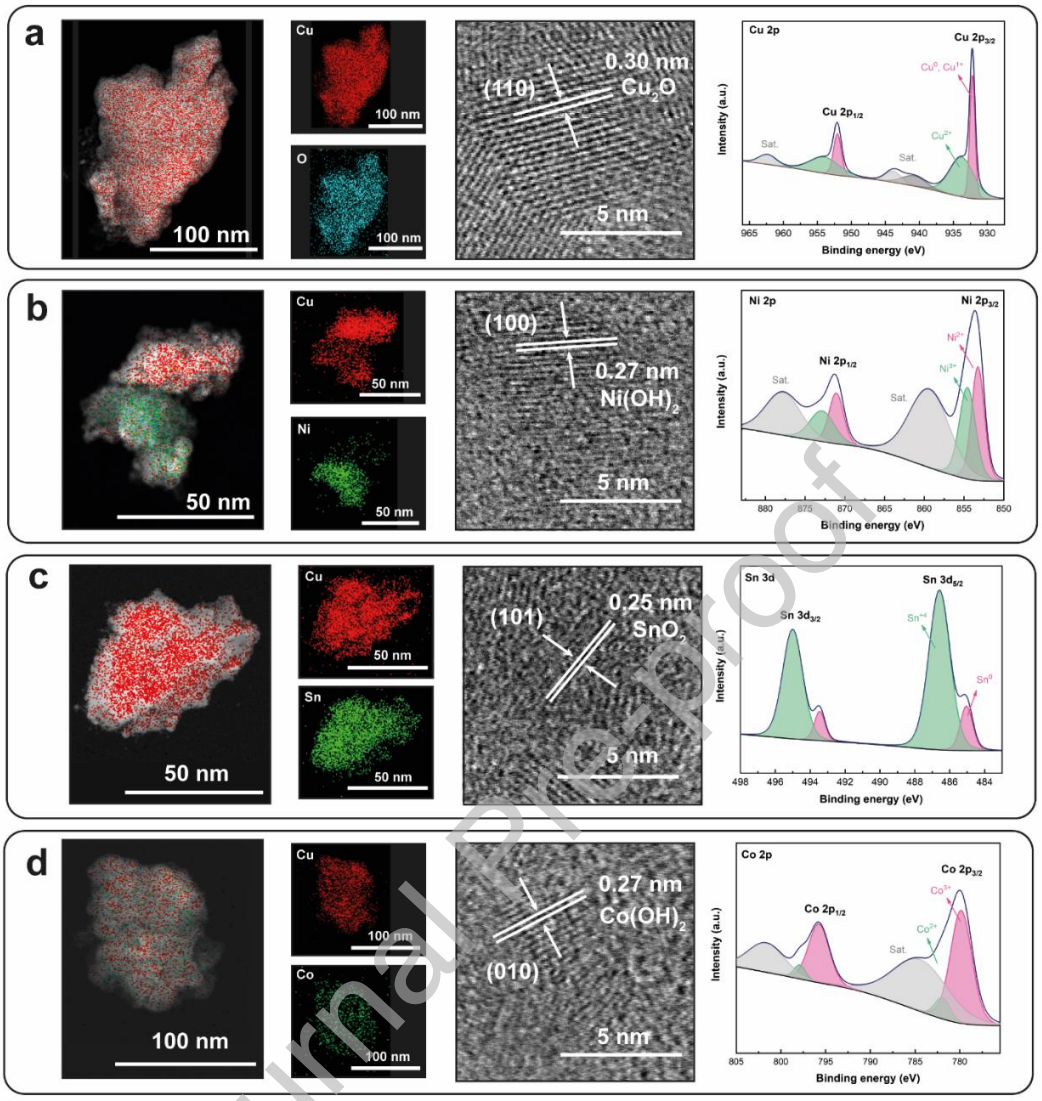


**Figure 3.** EDS mapping, BF-STEM images, and high-resolution XPS spectra for (a) $Cu/Cu_2O$, (b) $Cu/Ni(OH)_2$, (c) $Cu/SnO_2$, and (d) $Cu/Co(OH)_x$. Complete XPS analysis for each composition is available in the supplementary material as Figures S3-S6.

### *3.2. Bimetallic electrodes present different electrocatalytic intrinsic activity compared to Cu foam*

After generating bimetallic electrodes, the electrochemical surface area experienced changes in comparison to the pristine Cu foam. Therefore, evaluating the electrochemical surface area (ECSA) becomes crucial for evaluating the ERN response across different configurations. The ECSA is estimated through the electrical double-layer approach using a specific capacitance (e.g., 40 µF $cm^{-2}$), determined via cyclic voltammetry (CV) within a non-Faradaic current potential range e [62]. As illustrated in Figures

S7-S11 and summarized in Table S1, the calculated ECSA values for Cu foam, $Cu/Cu_2O$, $Cu/Ni(OH)_2$, $Cu/SnO_2$, and $Cu/Co(OH)_x$ are 5.58, 3.73, 5.75, 22.05, and 23.40 $cm^2$, respectively. These results demonstrate both minor and substantial deviations from the initial ECSA of pristine Cu foam. Such disparities could lead to either over or underestimation of the electrochemical responses since the non-Faradaic current of the real ECSA is not accounted for. Consequently, the experimental ECSA values were used to normalize the electrocatalytic responses in terms of current density (mA $cm_{ECSA}^{-2}$).

The electrocatalytic intrinsic activity was assessed by linear sweep voltammetry (LSV) in 12.5 mmol $L^{-1}$ $Na_2SO_4$ as support electrolyte, both in the absence and presence of 2 mmol $L^{-1}$ $NaNO_3$. Figure 4a illustrates the LSV of bare Cu foam, demonstrating a pronounced increase in current density in the presence of $NaNO_3$ in a range of -0.9 to -1.4 V vs Ag/AgCl. The highest current density difference, reaching -0.44 mA $cm_{ECSA}^{-2}$ occurs at -1.2 V vs Ag/AgCl, representing the specific potential for the ERN. Similarly, significant differences were observe for bimetallic electrodes (Figure S12), with values of -0.083, -0.15, -0.59, -0.74 mA $cm_{ECSA}^{-2}$ for $Cu/Ni(OH)_2$, $Cu/SnO_2$, $Cu/Cu_2O$, $Cu/Co(OH)_x$, respectively. Figure 4b presents the highest current density difference for each configuration at specific potentials (-1.3 and -1.2 V vs Ag/AgCl).

This evaluation indicates that modifying Cu with $Ni(OH)_2$ and $SnO_2$ nanocomposites decreases the intrinsic activity, resulting in a lower current density difference. On the other hand, modification with $Cu_2O$ and $Co(OH)_x$ enhances intrinsic activity, presenting a higher current density difference than Cu foam. Furthermore, this trend in intrinsic activity may reflect the performance of $NO_3^-$ conversion using the bimetallic electrodes.

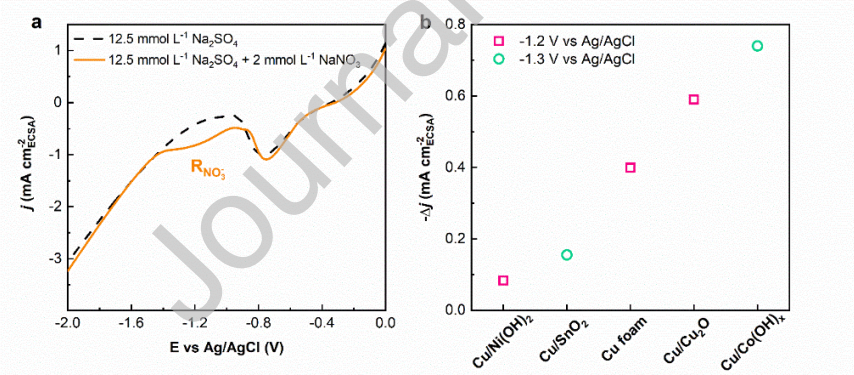


**Figure 4.** (a) LSV of Cu foam in the absence and presence of 2 mmol $NaNO_3$ with current density normalized by ECSA calculated. (b) Current density difference recorded in the absence and presence of $NaNO_3$ for bimetallic electrodes at the determined potential.

### *3.3. Bimetallic electrodes dominates the performance of ammonia production*

The bimetallic electrodes were tested under galvanostatic conditions maintaining a current density of 20 mA $cm^{-2}$ with an initial concentration of 30 mg $L^{-1}$ $NO_3^-$-N. The time-course mass balance of N-species for bare Cu foam (Figure S13) reveals a $NO_3^-$ conversion of 62.5 % after 240 min of treatment, resulting in a final concentration of 11.24 mg $L^{-1}$ $NO_3^-$-N. Notably, the maximum $NO_2^-$ peak production occurs at 90 min reaching 5.12 mg $L^{-1}$ $NO_2^-$-N, while $NH_3$ reaches 14.7 mg $L^{-1}$ $NH_3$-N by the end of the 240 min period.

The $NO_3^-$ conversion for $Cu/Cu_2O$ and $Cu/Ni(OH)_2$ (Figure 5a and 5b) after 240 min of electrolysis was 72.3 % and 29.3 %, respectively. In the case of $Cu/SnO_2$ (Figure 5c), the conversion reaches around 31.6% at 60 min without significant increase until 120 min. Conversely, $Cu/Co(OH)_x$ (Figure 5d) achieves 98.3 % conversion in the first 120 min. These results indicate that $Cu/Cu_2O$ and $Cu/Ni(OH)_2$ demonstrate continuous $NO_3^-$ conversion over time. In contrast, $Cu/SnO_2$ and $Cu/Co(OH)_x$ represents cases with sluggish and outstanding conversion, respectively.

Regarding $NO_2^-$ yield, $Cu/Cu_2O$ leads to the highest accumulation of undesired $NO_2^-$ (8.57 mg $L^{-1}$ $NO_2^-$-N) in 30 min of electrolysis, followed by 3.62, 1.71, and 1.15 mg $L^{-1}$ $NO_2^-$-N from $Cu/SnO_2$, $Cu/Ni(OH)_2$, and $Cu/Co(OH)_x$, respectively. Note that $NO_2^-$ is a more harmful contaminant than $NO_3^-$ with a maximum contaminant concentration limit of 1 mg $L^{-1}$ $NO_2^-$-N [63]. Therefore, electrodes with higher concentrations of $NO_2^-$ require further modification to completely reduce this N-species. For instance, the use of $Cu/Co(OH)_x$ achieves almost 99% conversion of $NO_3^-$ with negligible $NO_2^-$ concentration after 120 min of electrolysis.

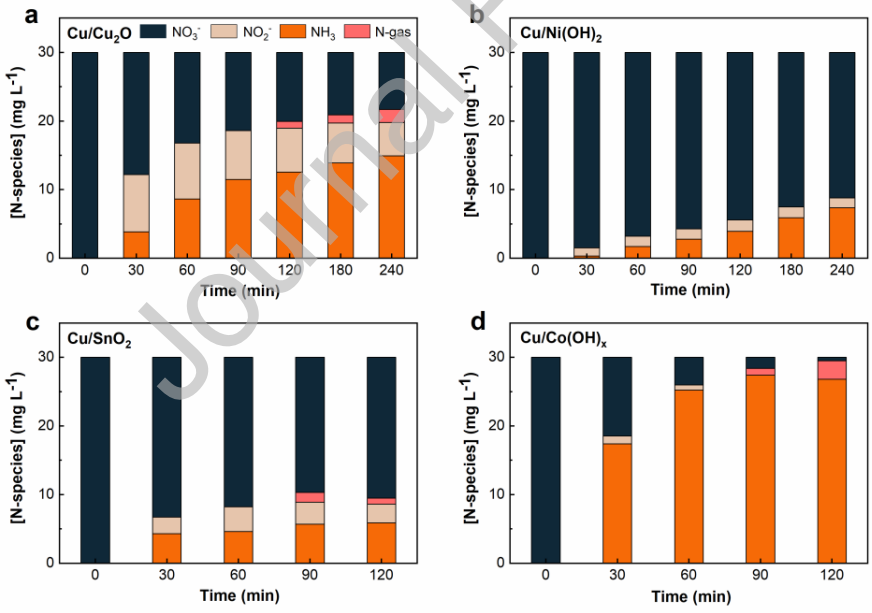


**Figure 5.** Time-course N-species mass balance during ERN at 20 mA $cm^{-2}$ using different bimetallic electrodes in 30 mg $L^{-1}$ $NO_3^-$-N (a) $Cu/Cu_2O$, (b) $Cu/Ni(OH)_2$, (c) $Cu/SnO_2$, and (d) $Cu/Co(OH)_x$.

To identify significant differences in conversion and time-course behavior of N-species after Cu foam modification, electrolysis experiments were conducted using an initial concentration of 30 mg $L^{-1}$

$NO_2^-$-N under identical conditions. Figure 6a illustrates the $NO_2^-$ concentration profiles over a 240 min electrolysis at 20 mA $cm^{-2}$ for different configurations. Employing a pseudo-first kinetic order as shown in Figure 6b, kinetic constants were calculated obtaining values of 1.4 x $10^{-2}$, 1.8 x $10^{-2}$, 25 x $10^{-2}$, 2.8 x $10^{-2}$, and 10.9 x $10^{-2}$ $min^{-1}$ for $Cu/SnO_2$, $Cu/Cu_2O$, $Cu/Ni(OH)_2$, Cu foam, and $Cu/Co(OH)_x$, respectively. The minimal values corresponding to $Cu/SnO_2$ and $Cu/Cu_2O$ materials demonstrate their low activity in converting $NO_2^-$, which explains the observed accumulation of $NO_2^-$. The sluggish activity of $SnO_2$ modification is related to the high solution pH ( ≥ 8) which promotes the formation of $Sn(OH)^+$ and $Sn(OH)_2$ inhibiting the adsorption of $NO_3^-$ at the electrode surface [39]. Meanwhile, the outstanding kinetics of $Cu/Co(OH)_x$ can account for the significant difference on $NO_2^-$ conversion kinetics observed among bimetallic configurations. Therefore, the mechanism can be explained by a two-step process, considering the rate-limiting step occurring over Cu sites (Equation (7)) and the subsequent reduction of $NO_2^-$ on Co sites (Equation (8)). These results underscore $Cu/Co(OH)_x$ as competitive bimetallic composition.

$$R_{NO_3^-} : NO_{3(ads)}^- + 2H^+ + 2e^- \rightarrow NO_{2(ads)}^- + H_2O \quad (7)$$

$$R_{NO_3^-} : NO_{2(ads)}^- + 7H^+ + 6e^- \rightarrow NH_3 + 2H_2O \quad (8)$$

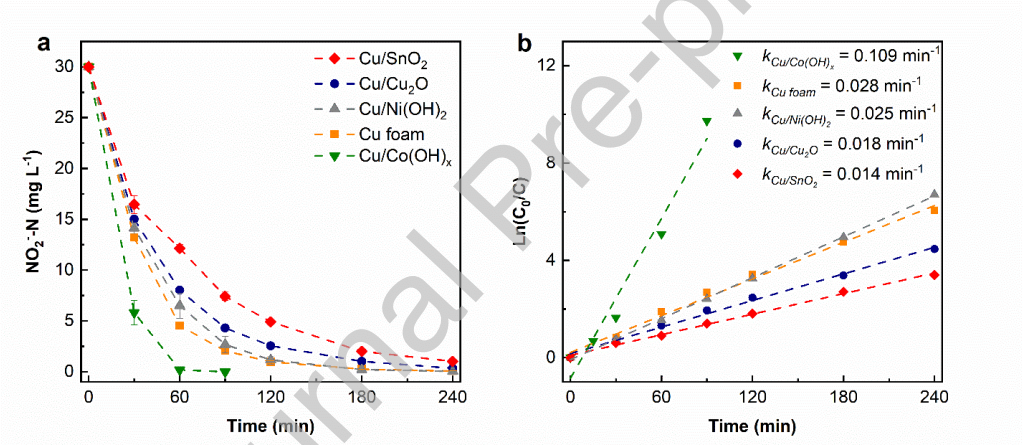


**Figure 6.** (a) Time-course concentration of initial 30 mg $L^{-1}$ $NO_2^-$-N at 20 mA $cm^{-2}$ using different electrode configurations. (b) Linear fit model for pseudo-first order reaction with calculated kinetic constants for the conversion of $NO_2^-$.

### *3.4. Figures of merit for bimetallic electrodes assess ammonia production*

Advancing towards higher technology readiness levels (TRL) involves transitioning from laboratory-scale research to the development stages, requiring validation under relevant conditions. Considering that existing electrochemical systems in the market operate under galvanostatic conditions (e.g., electrochlorination, electrocoating systems), assessing nitrate reduction under such conditions becomes a crucial step before further refining designs of electrochemical $NH_3$ generators. Therefore, determining the $NH_3$ yield obtained under different current densities to establish the *EE/O* and Faradaic efficiency under realistic operational settings is essential. These parameters are required for conducting techno-economic analysis and discussing the process feasibility across various boundary scenarios.

Figure 7 illustrates the $NH_3$ yield (mmol $NH_3$ $g_{cat}^{-1}$ $h^{-1}$) at different current densities for each bimetallic configuration. Starting from an initial 30 mg $L^{-1}$ $NO_3^-$-N, and assuming complete conversion with 100% selectivity towards ammonia within 2h of treatment using a standardized catalyst mass of 0.145 g, the maximum yield attainable is 0.74 mmol $NH_3$ $g_{cat}^{-1}$ $h^{-1}$. While selectivity performance can be overestimated due to dependency on the conversion levels reached, $NH_3$ generation efficiency offers a more comprehensive benchmarking tool, encompassing both the concepts of selectivity and conversion. For instance, $Cu/Cu_2O$ generates 12.4 mg $L^{-1}$ $NH_3$-N after 2 h, representing a selectivity to $NH_3$ of 62.8 % at 20 mA $cm^{-2}$. With and $NH_3$ yield of 0.28 mmol $NH_3$ $g_{cat}^{-1}$ $h^{-1}$, it represents a $NH_3$ generation efficiency of 35 %. This comparison highlights the $NH_3$ generation efficiency as a more reliable measure concerning $NH_3$ generation.

Similarly, $Cu/Ni(OH)_2$ reaches a maximum $NH_3$ yield of 0.21 mmol $NH_3$ $g_{cat}^{-1}$ $h^{-1}$ at 10 mA $cm^{-2}$, corresponding to 26.3 % $NH_3$ generation efficiency. $Cu/SnO_2$ configuration achieves a maximum $NH_3$ yield of 0.14 mmol $NH_3$ $g_{cat}^{-1}$ $h^{-1}$, with an $NH_3$ generation efficiency of 17.5 % at 20 mA $cm^{-2}$. While $NH_3$ generation efficiency remains low for the bimetallic $Cu/Cu_2O$, $Cu/Ni(OH)_2$, and $Cu/SnO_2$ due to low kinetics and $NO_2^-$ accumulation, $Cu/Co(OH)_x$ outperforms them. With a maximum $NH_3$ yield of 0.66 mmol $NH_3$ $g_{cat}^{-1}$ $h^{-1}$, $Cu/Co(OH)_x$ demonstrates an $NH_3$ generation efficiency of 89.1 % at 20 mA $cm^{-2}$. This outstanding performance can be attributed to the higher kinetics constant of $Co(OH)_x$ observed in the $NO_2^-$ reduction experiment. The $NH_3$ generation efficiency provides a better comparison between materials under identical experimental conditions, revealing the trend of $Cu/Co(OH)_x \geq Cu/Cu_2O \geq$ Cu foam $\geq Cu/SnO_2 \geq Cu/Ni(OH)_2$. While selectivity serves as a benchmarking parameter, indicating over 60% of selectivity for all configurations (see Table 1), $NH_3$ generation offers a more competitive assessment of each configuration.

The applied current density sets a related electrical potential on the electrodes. Measurements recorded using a multimeter and Ag/AgCl reference electrode indicate that at current densities 2.5 and 5 mA $cm^{-2}$, the electrical potential reached by the cathode across all configurations is lower than -1.6 V vs Ag/AgCl, confirming the low $NH_3$ yield due to low overpotential relative to $NO_3^-$ and $NO_2^-$ reduction potentials determined by LSV. However, at current densities exceeding 10 mA $cm^{-2}$, the cathode potential surpasses -2.2 V vs Ag/AgCl. Consequently, overpotential boosts the $NH_3$ yield at 10 mA $cm^{-2}$ and higher current densities until the hydrogen evolution reaction (HER) takes the primary role. Notably, $Cu/Co(OH)_x$ exhibits a unique behavior with current density increase, where $NH_3$ production increases, contrary to the other configurations tested. This can be attributed to the ability of $Co(OH)_x$ sites to adsorb atomic hydrogen which poses a high reductive potential demonstrated experimentally by electrochemical (e.g., Cyclic voltammetry), spectroscopy (e.g., electron spin resonance), and scavengers (e.g., tert-butyl alcohol) approaches [64–67]. Thus, the $Cu/Co(OH)_x$ configuration performs both direct and indirect reduction (Equations (9) – (15)), boosted by the atomic hydrogen adsorbed [28,42,68].

$$H_2O + 1e^- \rightarrow H_{(ads)} + OH^- \quad (9)$$

$$NO_{3(ads)}^- + 2H_{(ads)} \rightarrow NO_{2(ads)}^- + H_2O \quad (10)$$

$$NO_{2(ads)}^- + 1H_{(ads)} \rightarrow NO_{(ads)} + OH^- \quad (11)$$

$$NO_{(ads)} + 2H_{(ads)} \rightarrow N_{(ads)} + H_2O \quad (12)$$

$$N_{(ads)} + 1H_{(ads)} \rightarrow NH_{(ads)} \quad (13)$$

$$NH_{(ads)} + 1H_{(ads)} \rightarrow NH_{2(ads)} \quad (14)$$

$$NH_{2(ads)} + 1H_{(ads)} \rightarrow NH_{3(ads)} \quad (15)$$

The Faradaic efficiency (*FE*) for $NH_3$ generation represents the ratio between electrons supplied to the system and those used for $NH_3$ production. Generally, at a fixed potential, FE is high when a specific reaction occurs without any parallel reaction. However, under galvanostatic conditions the experimental potential changes depending on the applied current densities. Figure 7 presents the *FE* of each electrode at specific current densities. The HER for the bare Cu foam is around -1.1 V vs Ag/AgCl, with variations depending on the bimetallic surface (see Figure 4a and Figure S12). The maximum FE reached values of 14, 18, 8, and 41 % for $Cu/Cu_2O$, $Cu/Ni(OH)_2$, $Cu/SnO_2$, and $Cu/Co(OH)_x$, respectively.

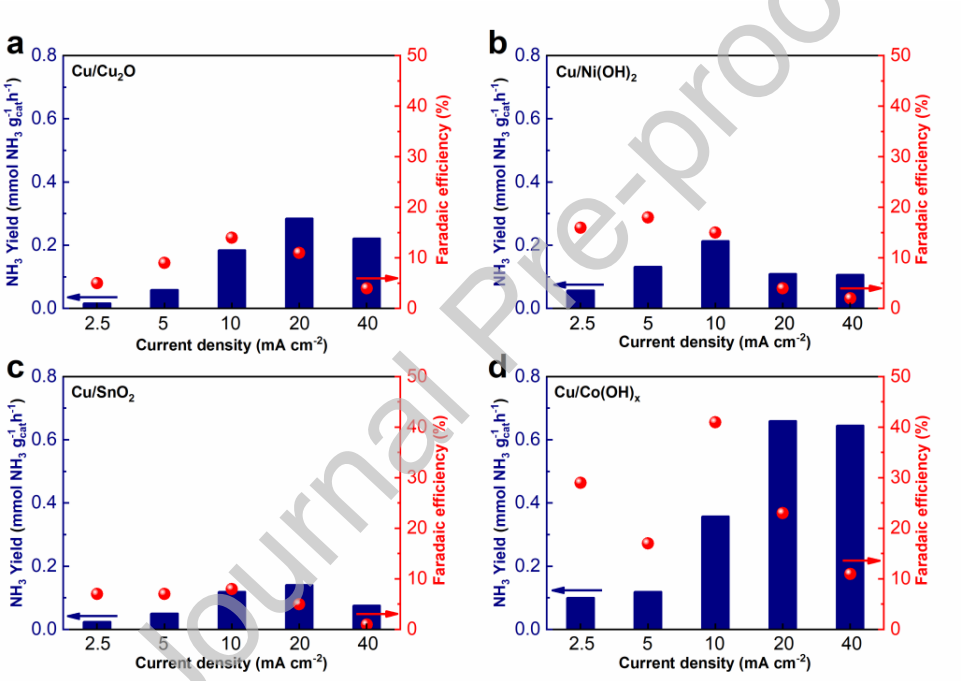


**Figure 7.** Ammonia yield (mmol $NH_3$ $g_{cat}^{-1}$ $h^{-1}$) and Faradic efficiency (%) after 2 h of electrolysis at different current densities (2.5, 5, 10, 20, and 40 mA $cm^{-2}$) using (a) $Cu/Cu_2O$, (b) $Cu/Ni(OH)_2$, (c) $Cu/SnO_2$, and (d) $Cu/Co(OH)_x$ electrodes for ERN in a 30 mg $L^{-1}$ $NO_3^-$-N solution.

The electrical energy per order (*EE/O*) represents the energy required to decrease the concentration of $NO_3^-$ by one order of magnitude, making kinetics for $NO_3^-$ conversion play an important role in energy consumption. Figure 8 depicts the kinetic constants calculated considering a pseudo-first order reaction and the corresponding *EE/O* values for specific configurations, including bare Cu foam. Compared to Cu foam, which has a kinetic constant of 6.3 x $10^{-3}$ $min^{-1}$ and *EE/O* of 44.5 kWh $m^{-3}$ $order^{-1}$, $Cu/Ni(OH)_2$ and $Cu/SnO_2$ present a kinetic constants of 1.79 x $10^{-3}$ $min^{-1}$ and 4.25 x $10^{-3}$ $min^{-1}$ resulting in *EE/O* values of 192 and 127 kWh $m^{-3}$ $order^{-1}$, respectively. Meanwhile, $Cu/Cu_2O$ and $Cu/Co(OH)_x$ display

kinetic constants of 8.21 x $10^{-3}$ $min^{-1}$ and 33.8 x $10^{-3}$ $min^{-1}$, yielding *EE/O* values of 39.0 and 11.0 kWh $m^{-3}$ $order^{-1}$, respectively. One of the key findings is the high activity of $Cu/Co(OH)_x$ with superior $NH_3$ generation efficiency at lower energy consumption compared to other configurations. Table 1 summarizes the significant revelations for all configurations, including $NO_3^-$ conversion, $NH_3$ selectivity, generation efficiency, $NH_3$ yield, Faradaic efficiency, kinetics constant, and electrical energy per order. These results suggest that bimetallic materials harnessing the synergies of indirect reduction through hydrogenation (i.e., $Cu/Co(OH)_x$) hold promise for boosting performance under galvanostatic operation while enhancing selectivity of ammonia production with reduce energy demands.

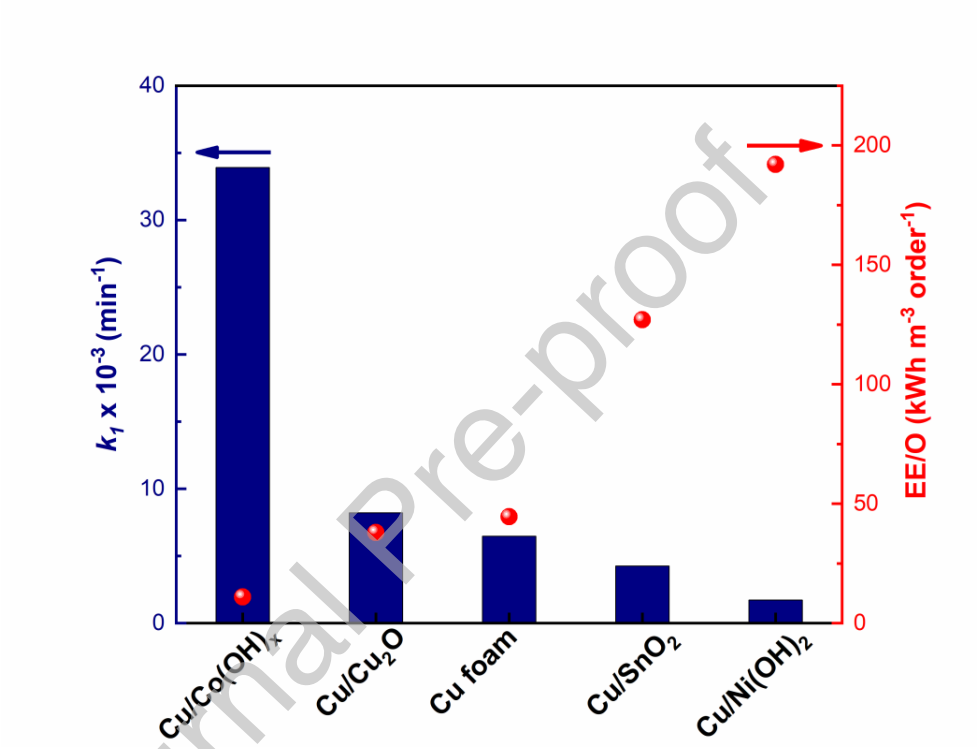


**Figure 8.** Pseudo-first order kinetic constant for $NO_3^-$ conversion ($min^{-1}$) and the electric energy per order (EE/O - kWh $m^{-3}$ $order^{-1}$) for bare Cu foam, $Cu/Cu_2O$, $Cu/SnO_2$, $Cu/Ni(OH)_2$, and $Cu/Co(OH)_x$.

**Table 1.** Performance parameters of bimetallic electrodes for the electrochemical $NH_3$ generation from initial 30 mg $L^{-1}$ $NO_3^-$-N under 20 mA $cm^{-2}$ for 2 h including nitrate conversion (*NC*), ammonia selectivity ($S_{NH3}$), ammonia generation efficiency (*GE*), ammonia maximum yield ($Yield_{max}$), Faradaic efficiency (*FE*), pseudo-first order kinetic rate constant ($k_1$), and electrical energy per order (*EE/O*).

| Electrode | *NC* (%) | $S_{NH3}$ (%) | *GE* (%) | $NH_3$ $Yield_{max}$ (mmol $NH_3$ $g_{cat}^{-1}$ $h^{-1}$) | *FE* (%) | $k_1$ ($min^{-1}$) | *EE/O* (kWh $m^{-3}$ $order^{-1}$) |
|---|---|---|---|---|---|---|---|
| **Cu foam** | 54 | 70.1 | 37.8 | 0.28 | 10 | 6.3 x $10^{-3}$ | 44.5 |

| | | | | | | | |
|---|---|---|---|---|---|---|---|
| **$Cu/Cu_2O$** | 66.5 | 62.8 | 40.5 | 0.30 | 11 | $8.2 \times 10^{-3}$ | 38 |
| **$Cu/Ni(OH)_2$** | 18.6 | 69.8 | 13.5 | 0.10 | 4 | $1.7 \times 10^{-3}$ | 192 |
| **$Cu/SnO_2$** | 31.6 | 62.1 | 18.9 | 0.14 | 5 | $4.2 \times 10^{-3}$ | 127 |
| **$Cu/Co(OH)_x$** | 98.3 | 91 | 89.1 | 0.66 | 23 | $33 \times 10^{-3}$ | 11 |

**4. Conclusions**

This study evaluates bimetallic earth-abundant electrodes for electrochemical reduction of nitrate, employing environmentally relevant concentrations of 30 mg $L^{-1}$ $NO_3^-$-N and 12.5 mmol $L^{-1}$ $Na_2SO_4$ under galvanostatic conditions. The electrodes $Cu/Cu_2O$, $Cu/Ni(OH)_2$, $Cu/SnO_2$, and $Co(OH)_x$ were synthesized over 110 PPI Cu foam by a simple electrodeposition method and then thoroughly characterized. Evaluation of intrinsic activity via linear sweep voltammetry reveals the following trend for $NO_3^-$ reduction: $Cu/Co(OH)_x$ > $Cu/Cu_2O$ > Cu foam > $Cu/SnO_2$ > $Cu/Ni(OH)_2$. Electrolysis at 20 mA $cm^{-2}$ validates this trend, with Cu foam, $Cu/Cu_2O$, and $Cu/Ni(OH)_2$ exhibiting continuous conversion over time accompanied by $NO_2^-$accumulation in solution, while $Cu/SnO_2$ faces challenges in conversion after 1 h of electrolysis. Conversely, $Cu/Co(OH)_x$ demonstrates superior conversion and $NH_3$ generation efficiency compared to other configurations. Electrolysis of 30 mg $L^{-1}$ $NO_2^-$N at 20 mA $cm^{-2}$ for 2 h evaluates the capability to reduce the $NO_2^-$, revealing a kinetic constant trend of $Cu/Co(OH)_x$ > Cu foam > $Cu/Ni(OH)_2$ > $Cu/Cu_2O$ > $Cu/SnO_2$.Evaluation of current densities determines optimal conditions for $NH_3$ yield, considering the Faradaic efficiency, $NH_3$ generation efficiency, and electrical energy per order. These findings shed light on electrocatalysis performed under galvanostatic conditions and inform the logical design of electrocatalysts using earth-abundant materials. The identification of electrocatalytic materials capable of exploiting parasitic HER reaction to stabilize strong reductant Hads appears as essential for enhancing the performance of galvanostatic systems. Enabling indirect electrochemical reduction processes holds promise for synergistically leveraging a once-considered parasitic reaction to facilitate a low energy. high-selectivity transformation of nitrate into ammonia through simultaneous electrocatalytic hydrogenation mechanisms.

**Acknowledgments**

This project has received funding from the Herman Frasch Fund for Chemical Research, Bank of America, N.A., Trustee with grant number G10224-300. and from the European Union's Horizon 2020 research and innovation program under the Marie Skłodowska-Curie grant agreement No 843870. A. S. Fajardo is grateful to the FCT- Foundation for Science and Technology, P.I., for the financial support granted under the institutional scientific employment program-contract (CEECINST/00077/2021) and through national funds to the research unit Research Centre for Natural Resources, Environment and Society—CERNAS (https://doi.org/10.54499/UIDP/00681/2020). This research is also based upon research supported by

the Transatlantic Research Partnership of the Embassy of France in the United States and the FACE Foundation. The authors acknowledge the support of the Centre National de la Recherche Scientifique (CNRS). D. Leon and S. Garcia-Segura thank the support of National Science Foundation (NSF) Cooperative Agreement No. HRD-1619524 Louis Stokes Renewal STEM Pathways and Research Alliance: Western Alliance to Expand Student Opportunities- Advancing Institutionalization for STEM Leadership Expansion (WAESO-AISLE)", funded through the National Science Foundation Division of Equity for Excellence in STEM, Award Number: 2207398. We acknowledge the use of facilities within the Eyring Materials Center at Arizona State University, supported partly by NNCI-ECCS -2025490.

**References**


[1] U. Nations, Peace, dignity and equality on a healthy planet: Population, United Nations. (2023). https://www.un.org/en/global-issues/population.

[2] Erisman, Nitrogen Demand, Glob. Chang. Biol. 14 (2008) 2057–2063.

[3] D.R. MacFarlane, P. V. Cherepanov, J. Choi, B.H.R. Suryanto, R.Y. Hodgetts, J.M. Bakker, F.M. Ferrero Vallana, A.N. Simonov, A Roadmap to the Ammonia Economy, Joule. 4 (2020) 1186–1205. https://doi.org/10.1016/j.joule.2020.04.004.

[4] J. Brightling, Ammonia and the fertiliser industry: The development of ammonia at Billingham, Johnson Matthey Technol. Rev. 62 (2018) 32–47. https://doi.org/10.1595/205651318X696341.

[5] K. Verleysen, A. Parente, F. Contino, How does a resilient, flexible ammonia process look? Robust design optimization of a Haber-Bosch process with optimal dynamic control powered by wind, Proc. Combust. Inst. 39 (2023) 5511–5520. https://doi.org/10.1016/j.proci.2022.06.027.

[6] B. Lin, F.H. Nowrin, J.J. Rosenthal, A.S. Bhown, M. Malmali, Perspective on Intensification of Haber−Bosch to Enable Ammonia Production under Milder Conditions, ACS Sustain. Chem. Eng. 11 (2023) 9880–9899. https://doi.org/10.1021/acssuschemeng.2c06711.

[7] C. Wang, S.D.C. Walsh, T. Longden, G. Palmer, I. Lutalo, R. Dargaville, Optimising renewable generation configurations of off-grid green ammonia production systems considering Haber-Bosch flexibility, Energy Convers. Manag. 280 (2023) 116790. https://doi.org/10.1016/j.enconman.2023.116790.

[8] C.A. Fernandez, M.C. Hatzell, Editors' Choice—Economic Considerations for Low-Temperature Electrochemical Ammonia Production: Achieving Haber-Bosch Parity, J. Electrochem. Soc. 167 (2020) 143504. https://doi.org/10.1149/1945-7111/abc35b.

[9] A.J. dos Santos, H.L. Barazorda-Ccahuana, G. Caballero-Manrique, Y. Chérémond, P.J. Espinoza-Montero, J.R. González-Rodríguez, U.J. Jáuregui-Haza, M.R.V. Lanza, A. Nájera, C. Oporto, A. Pérez Parada, T. Pérez, V.D. Quezada, V. Rojas, V. Sosa, A. Thiam, R.A. Torres-Palma, R. Vargas, S. Garcia-Segura, Accelerating innovative water treatment in Latin America, Nat. Sustain. (2023). https://doi.org/10.1038/s41893-022-01042-z.

[10] X. Lu, H. Song, J. Cai, S. Lu, Recent development of electrochemical nitrate reduction to ammonia: A mini review, Electrochem. Commun. 129 (2021) 107094. https://doi.org/10.1016/j.elecom.2021.107094.

[11] Y. Gao, R. Wang, Y. Li, E. Han, M. Song, Z. Yang, F. Guo, Y. He, X. Yang, Regulating dynamic equilibrium of active hydrogen for super-efficient nitrate electroreduction to ammonia, Chem. Eng. J. 474 (2023) 145546. https://doi.org/10.1016/j.cej.2023.145546.

[12] P.H. van Langevelde, I. Katsounaros, M.T.M. Koper, Electrocatalytic Nitrate Reduction for

Sustainable Ammonia Production, Joule. 5 (2021) 290–294. https://doi.org/10.1016/j.joule.2020.12.025.

[13] J. Martínez, A. Ortiz, I. Ortiz, State-of-the-art and perspectives of the catalytic and electrocatalytic reduction of aqueous nitrates, Appl. Catal. B Environ. 207 (2017) 42–59. https://doi.org/10.1016/j.apcatb.2017.02.016.

[14] S. Garcia-Segura, M. Lanzarini-Lopes, K. Hristovski, P. Westerhoff, Electrocatalytic reduction of nitrate: Fundamentals to full-scale water treatment applications, Appl. Catal. B Environ. 236 (2018) 546–568. https://doi.org/10.1016/j.apcatb.2018.05.041.

[15] G.F. Chen, Y. Yuan, H. Jiang, S.Y. Ren, L.X. Ding, L. Ma, T. Wu, J. Lu, H. Wang, Electrochemical reduction of nitrate to ammonia via direct eight-electron transfer using a copper–molecular solid catalyst, Nat. Energy. 5 (2020) 605–613. https://doi.org/10.1038/s41560-020-0654-1.

[16] A.S. Fajardo, P. Westerhoff, C.M. Sanchez-Sanchez, S. Garcia-Segura, Earth-abundant elements a sustainable solution for electrocatalytic reduction of nitrate, Appl. Catal. B Environ. 281 (2021) 119465. https://doi.org/10.1016/j.apcatb.2020.119465.

[17] A.S. Fajardo, P. Westerhoff, S. Garcia-Segura, C.M. Sánchez-Sánchez, Selectivity modulation during electrochemical reduction of nitrate by electrolyte engineering, Sep. Purif. Technol. 321 (2023) 124233. https://doi.org/10.1016/j.seppur.2023.124233.

[18] S. Guo, H. Li, K.N. Heck, X. Luan, W. Guo, G. Henkelman, M.S. Wong, Gold boosts nitrate reduction and deactivation resistance to indium-promoted palladium catalysts, Appl. Catal. B Environ. 305 (2022) 121048. https://doi.org/10.1016/j.apcatb.2021.121048.

[19] Z. Wang, S.D. Young, B.R. Goldsmith, N. Singh, Increasing electrocatalytic nitrate reduction activity by controlling adsorption through PtRu alloying, J. Catal. 395 (2021) 143–154. https://doi.org/10.1016/j.jcat.2020.12.031.

[20] J.X. Liu, D. Richards, N. Singh, B.R. Goldsmith, Activity and Selectivity Trends in Electrocatalytic Nitrate Reduction on Transition Metals, ACS Catal. 9 (2019) 7052–7064. https://doi.org/10.1021/acscatal.9b02179.

[21] M.S. El-Deab, Electrochemical reduction of nitrate to ammonia at modified gold electrodes, Electrochim. Acta. 49 (2004) 1639–1645. https://doi.org/10.1016/j.electacta.2003.11.025.

[22] F. Gauthard, F. Epron, J. Barbier, Palladium and platinum-based catalysts in the catalytic reduction of nitrate in water: Effect of copper, silver, or gold addition, J. Catal. 220 (2003) 182–191. https://doi.org/10.1016/S0021-9517(03)00252-5.

[23] M. Liu, Q. Mao, K. Shi, Z. Wang, Y. Xu, X. Li, L. Wang, H. Wang, Electroreduction of Nitrate to Ammonia on Palladium-Cobalt-Oxygen Nanowire Arrays, ACS Appl. Mater. Interfaces. 14 (2022) 13169–13176. https://doi.org/10.1021/acsami.1c19412.

[24] J. Lim, C.Y. Liu, J. Park, Y.H. Liu, T.P. Senftle, S.W. Lee, M.C. Hatzell, Structure Sensitivity of Pd Facets for Enhanced Electrochemical Nitrate Reduction to Ammonia, ACS Catal. 11 (2021) 7568–7577. https://doi.org/10.1021/acscatal.1c01413.

[25] C.A. Clark, C.P. Reddy, H. Xu, K.N. Heck, G. Luo, T.P. Senftle, M.S. Wong, Mechanistic insights into ph-controlled nitrite reduction to ammonia and hydrazine over rhodium, ACS Catal. 10 (2020) 494–509. https://doi.org/10.1021/acscatal.9b03239.

[26] C.J. Rhodes, Endangered elements, critical raw materials and conflict minerals, 2019. https://doi.org/10.1177/0036850419884873.

[27] K. Flores, G.A. Cerrón-Calle, C. Valdes, A. Atrashkevich, A. Castillo, H. Morales, J.G. Parsons, S. Garcia-Segura, J.L. Gardea-Torresdey, Outlining Key Perspectives for the Advancement of Electrocatalytic Remediation of Nitrate from Polluted Waters, ACS ES&T Eng. 2 (2022) 746–768. https://doi.org/10.1021/acsestengg.2c00052.

[28] M.A. Hasnat, M.A. Rashed, S. Ben Aoun, S.M.N. Uddin, M. Saiful Alam, S. Amertharaj, R.K. Majumder, N. Mohamed, Dissimilar catalytic trails of nitrate reduction on Cu-modified Pt surface immobilized on H+ conducting solid polymer, J. Mol. Catal. A Chem. 383–384 (2014) 243–248. https://doi.org/10.1016/j.molcata.2013.12.015.

[29] S. Zhang, M. Li, J. Li, Q. Song, X. Liu, High-ammonia selective metal – organic framework – derived Co-doped Fe / Fe 2 O 3 catalysts for electrochemical nitrate reduction, 119 (2022) 2115504119. https://doi.org/https://doi.org/10.1073/pnas.2115504119.

[30] W. Fu, Y. Du, J. Jing, C. Fu, M. Zhou, Highly selective nitrate reduction to ammonia on CoO/Cu foam via constructing interfacial electric field to tune adsorption of reactants, Appl. Catal. B Environ. 324 (2023) 122201. https://doi.org/10.1016/j.apcatb.2022.122201.

[31] X. Fan, C. Ma, D. Zhao, Z. Deng, L. Zhang, Y. Wang, Y. Luo, D. Zheng, T. Li, J. Zhang, S. Sun, Q. Lu, X. Sun, Unveiling selective nitrate reduction to ammonia with Co3O4 nanosheets/TiO2 nanobelt heterostructure catalyst, J. Colloid Interface Sci. 630 (2023) 714–720. https://doi.org/10.1016/j.jcis.2022.10.050.

[32] Y.J. Shih, Z.L. Wu, Y.H. Huang, C.P. Huang, Electrochemical nitrate reduction as affected by the crystal morphology and facet of copper nanoparticles supported on nickel foam electrodes (Cu/Ni), Chem. Eng. J. 383 (2020) 123157. https://doi.org/10.1016/j.cej.2019.123157.

[33] M. Marcos-Hernández, G. Antonio Cerrón-Calle, Y. Ge, S. Garcia-Segura, C.M. Sánchez-Sánchez, A.S. Fajardo, D. Villagrán, Effect of surface functionalization of Fe3O4 nano-enabled electrodes on the electrochemical reduction of nitrate, Sep. Purif. Technol. 282 (2022) 119771. https://doi.org/10.1016/j.seppur.2021.119771.

[34] G.A. Cerrón-Calle, T.P. Senftle, S. Garcia-Segura, Strategic tailored design of electrocatalysts for environmental remediation based on density functional theory (DFT) and microkinetic modeling,

Curr. Opin. Electrochem. 35 (2022) 101062. https://doi.org/10.1016/j.coelec.2022.101062.

[35] Y. Wang, W. Zhou, R. Jia, Y. Yu, B. Zhang, Unveiling the Activity Origin of a Copper-based Electrocatalyst for Selective Nitrate Reduction to Ammonia, Angew. Chemie - Int. Ed. 59 (2020) 5350–5354. https://doi.org/10.1002/anie.201915992.

[36] Q. Gao, H.S. Pillai, Y. Huang, S. Liu, Q. Mu, X. Han, Z. Yan, H. Zhou, Q. He, H. Xin, H. Zhu, Breaking adsorption-energy scaling limitations of electrocatalytic nitrate reduction on intermetallic CuPd nanocubes by machine-learned insights, Nat. Commun. 13 (2022) 1–12. https://doi.org/10.1038/s41467-022-29926-w.

[37] Y. Wang, A. Xu, Z. Wang, L. Huang, J. Li, F. Li, J. Wicks, M. Luo, D.H. Nam, C.S. Tan, Y. Ding, J. Wu, Y. Lum, C.T. Dinh, D. Sinton, G. Zheng, E.H. Sargent, Enhanced Nitrate-to-Ammonia Activity on Copper-Nickel Alloys via Tuning of Intermediate Adsorption, J. Am. Chem. Soc. 142 (2020) 5702–5708. https://doi.org/10.1021/jacs.9b13347.

[38] B.K. Simpson, D.C. Johnson, Electrocatalysis of nitrate reduction at copper-nickel alloy electrodes in acidic media, Electroanalysis. 16 (2004) 532–538. https://doi.org/10.1002/elan.200302790.

[39] Y. Deng, M. Kato, J. Zheng, C. Feng, I. Yagi, The pH dependence of the electrocatalytic nitrate reduction by tin-modified palladium(100) electrodes: Effects of structures of tin species and protonation of nitrite, Electrochim. Acta. 470 (2023) 143301. https://doi.org/10.1016/j.electacta.2023.143301.

[40] K. Shimazu, R. Goto, K. Tada, Electrochemical reduction of nitrate ions on tin-modified platinum and palladium electrodes, Chem. Lett. (2002) 204–205. https://doi.org/10.1246/cl.2002.204.

[41] M. Kato, M. Okui, S. Taguchi, I. Yagi, Electrocatalytic nitrate reduction on well-defined surfaces of tin-modified platinum, palladium and platinum-palladium single crystalline electrodes in acidic and neutral media, J. Electroanal. Chem. 800 (2017) 46–53. https://doi.org/10.1016/j.jelechem.2017.01.020.

[42] Y. Xu, W. Sun, J. Cheng, X. Yang, G. Dai, J. Liu, Enhancing hydrogenation with Co/Cu foam electrode to achieve wide-range electroreduction of nitrate to ammonia, Electrochim. Acta. 472 (2023) 143348. https://doi.org/10.1016/j.electacta.2023.143348.

[43] S.S. Shi, Z.X. Yuan, F. Zhang, P. Chen, A Co3O4-x/Co nanocomposite with synergistically enhanced electrochemical activity for reduction of nitrite to ammonia, Electrochim. Acta. 473 (2024) 143455. https://doi.org/10.1016/j.electacta.2023.143455.

[44] G.A. Cerrón-Calle, A.S. Fajardo, J. Liu, C.M. Sánchez-Sánchez, S. Garcia-Segura, Enabling circular economy by N-recovery: Electrocatalytic reduction of nitrate with cobalt hydroxide nanocomposites on copper foam treating low conductivity groundwater effluents, Sci. Total Environ. 887 (2023) 163938. https://doi.org/10.1016/j.scitotenv.2023.163938.

[45] Daily Metal Prices, Dly. Met. Spot Prices. (2024). https://www.dailymetalprice.com/metalprices.php.

[46] X. Zhang, Y. Wang, C. Liu, Y. Yu, S. Lu, B. Zhang, Recent advances in non-noble metal electrocatalysts for nitrate reduction, Chem. Eng. J. 403 (2021) 126269. https://doi.org/10.1016/j.cej.2020.126269.

[47] D. Liu, L. Qiao, S. Peng, H. Bai, C. Liu, W.F. Ip, K.H. Lo, H. Liu, K.W. Ng, S. Wang, X. Yang, H. Pan, Recent Advances in Electrocatalysts for Efficient Nitrate Reduction to Ammonia, Adv. Funct. Mater. 2303480 (2023) 1–31. https://doi.org/10.1002/adfm.202303480.

[48] K. Zuo, S. Garcia-Segura, G.A. Cerrón-Calle, F.Y. Chen, X. Tian, X. Wang, X. Huang, H. Wang, P.J.J. Alvarez, J. Lou, M. Elimelech, Q. Li, Electrified water treatment: fundamentals and roles of electrode materials, Nat. Rev. Mater. 2023. 8 (2023) 472–490. https://doi.org/10.1038/s41578-023-00564-y.

[49] H. Liu, J. Li, F. Du, L. Yang, S. Huang, J. Gao, C. Li, C. Guo, A core–shell copper oxides-cobalt oxides heterostructure nanowire arrays for nitrate reduction to ammonia with high yield rate, Green Energy Environ. (2022). https://doi.org/10.1016/j.gee.2022.03.003.

[50] S.Y. Zhen, H.T. Wu, Y. Wang, N. Li, H. Sen Chen, W.L. Song, Z.H. Wang, W. Sun, K.N. Sun, Metal-organic framework derived hollow porous CuO-CuCo2O4 dodecahedrons as a cathode catalyst for Li-O2 batteries, RSC Adv. 9 (2019) 16288–16295. https://doi.org/10.1039/c9ra02860a.

[51] X. Zhang, Q. Lin, H. Luo, R. Huang, R. Xiao, Q. Liu, Activation of persulfate with 3D urchin-like CoO-CuO microparticles for DBP degradation: A catalytic mechanism study, Sci. Total Environ. 655 (2019) 614–621. https://doi.org/10.1016/j.scitotenv.2018.11.281.

[52] L. Yang, J. Li, F. Du, J. Gao, H. Liu, S. Huang, H. Zhang, C. Li, C. Guo, Interface engineering cerium-doped copper nanocrystal for efficient electrochemical nitrate-to-ammonia production, Electrochim. Acta. 411 (2022) 140095. https://doi.org/10.1016/j.electacta.2022.140095.

[53] Y. Xu, K. Ren, T. Ren, M. Wang, Z. Wang, X. Li, L. Wang, H. Wang, Ultralow-content Pd in-situ incorporation mediated hierarchical defects in corner-etched Cu2O octahedra for enhanced electrocatalytic nitrate reduction to ammonia, Appl. Catal. B Environ. 306 (2022) 121094. https://doi.org/10.1016/j.apcatb.2022.121094.

[54] X. Wang, J. Hu, Y. Su, J. Hao, F. Liu, S. Han, J. An, J. Lian, Ni Foam-Ni3S2@Ni(OH)2-Graphene Sandwich Structure Electrode Materials: Facile Synthesis and High Supercapacitor Performance, Chem. - A Eur. J. 23 (2017) 4128–4136. https://doi.org/10.1002/chem.201605212.

[55] Y. Yang, H. Wang, L. Wang, Y. Ge, K. Kan, K. Shi, J. Chen, A novel gas sensor based on porous α-Ni(OH)2 ultrathin nanosheet/reduced graphene oxide composites for room temperature detection of NO:X, New J. Chem. 40 (2016) 4678–4686. https://doi.org/10.1039/c5nj03284a.

[56] Z. Huang, J. Zhu, Y. Hu, Y. Zhu, G. Zhu, L. Hu, Y. Zi, W. Huang, Tin Oxide (SnO2) Nanoparticles: Facile Fabrication, Characterization, and Application in UV Photodetectors, Nanomaterials. 12 (2022). https://doi.org/10.3390/nano12040632.

[57] N. Kamboj, B. Debnath, S. Bhardwaj, T. Paul, N. Kumar, S. Ogale, K. Roy, R.S. Dey, Ultrafine Mix-Phase SnO-SnO2Nanoparticles Anchored on Reduced Graphene Oxide Boost Reversible Li-Ion Storage Capacity beyond Theoretical Limit, ACS Nano. 16 (2022) 15358–15368. https://doi.org/10.1021/acsnano.2c07008.

[58] W. Wang, X. Duan, X. Sui, Q. Wang, F. Xu, L. Chang, Surface characterization and electrochemical properties of PbO2/SnO2 composite anodes for electrocatalytic oxidation of m-nitrophenol, Electrochim. Acta. 335 (2020) 135649. https://doi.org/10.1016/j.electacta.2020.135649.

[59] Z. Wang, H. Wang, S. Ji, X. Wang, B.G. Pollet, R. Wang, Multidimensional regulation of Ni3S2@Co(OH)2 catalyst with high performance for wind energy electrolytic water, J. Power Sources. 446 (2020) 227348. https://doi.org/10.1016/j.jpowsour.2019.227348.

[60] Y. Dou, D. Yuan, L. Yu, W. Zhang, L. Zhang, K. Fan, M. Al-Mamun, P. Liu, C.T. He, H. Zhao, Interpolation between W Dopant and Co Vacancy in CoOOH for Enhanced Oxygen Evolution Catalysis, Adv. Mater. 34 (2022) 1–9. https://doi.org/10.1002/adma.202104667.

[61] S. Ye, J. Wang, J. Hu, Z. Chen, L. Zheng, Y. Fu, Y. Lei, X. Ren, C. He, Q. Zhang, J. Liu, Electrochemical Construction of Low-Crystalline CoOOH Nanosheets with Short-Range Ordered Grains to Improve Oxygen Evolution Activity, ACS Catal. 11 (2021) 6104–6112. https://doi.org/10.1021/acscatal.1c01300.

[62] D.M. Morales, M. Risch, Seven steps to reliable cyclic voltammetry measurements for the determination of double layer capacitance, JPhys Energy. 3 (2021) 034013. https://doi.org/10.1088/2515-7655/abee33.

[63] M.J. Pennino, J.E. Compton, S.G. Leibowitz, Trends in Drinking Water Nitrate Violations Across the United States, Environ. Sci. Technol. 51 (2017) 13450–13460. https://doi.org/10.1021/acs.est.7b04269.

[64] B. Xu, Z. Chen, G. Zhang, Y. Wang, On-Demand Atomic Hydrogen Provision by Exposing Electron-Rich Cobalt Sites in an Open-Framework Structure toward Superior Electrocatalytic Nitrate Conversion to Dinitrogen, Environ. Sci. Technol. (2021). https://doi.org/10.1021/acs.est.1c06091.

[65] W. Fu, Y. Du, J. Jing, C. Fu, M. Zhou, Highly selective nitrate reduction to ammonia on CoO/Cu foam via constructing interfacial electric field to tune adsorption of reactants, Appl. Catal. B Environ. 324 (2023) 122201. https://doi.org/10.1016/j.apcatb.2022.122201.

[66] G.A. Cerrón-Calle, A. Wines, S. Garcia-Segura, Atomic hydrogen provision by cobalt sites in a bimetallic Ni/Co(OH)x and trimetallic Ni/Cu2O/Co(OH)x configurations for superior ammonia production, Appl. Catal. B Environ. 328 (2023) 122540.

https://doi.org/10.1016/j.apcatb.2023.122540.

[67] Y. Yu, C. Wang, Y. Yu, Y. Wang, B. Zhang, Promoting selective electroreduction of nitrates to ammonia over electron-deficient Co modulated by rectifying Schottky contacts, Sci. China Chem. 63 (2020) 1469–1476. https://doi.org/10.1007/s11426-020-9795-x.

[68] Z. Niu, S. Fan, X. Li, Z. Liu, J. Wang, J. Duan, M.O. Tadé, S. Liu, Facile Tailoring of the Electronic Structure and the d-Band Center of Copper-Doped Cobaltate for Efficient Nitrate Electrochemical Hydrogenation, ACS Appl. Mater. Interfaces. 14 (2022) 35477–35484. https://doi.org/10.1021/acsami.2c04789.



## Graphical Abstract

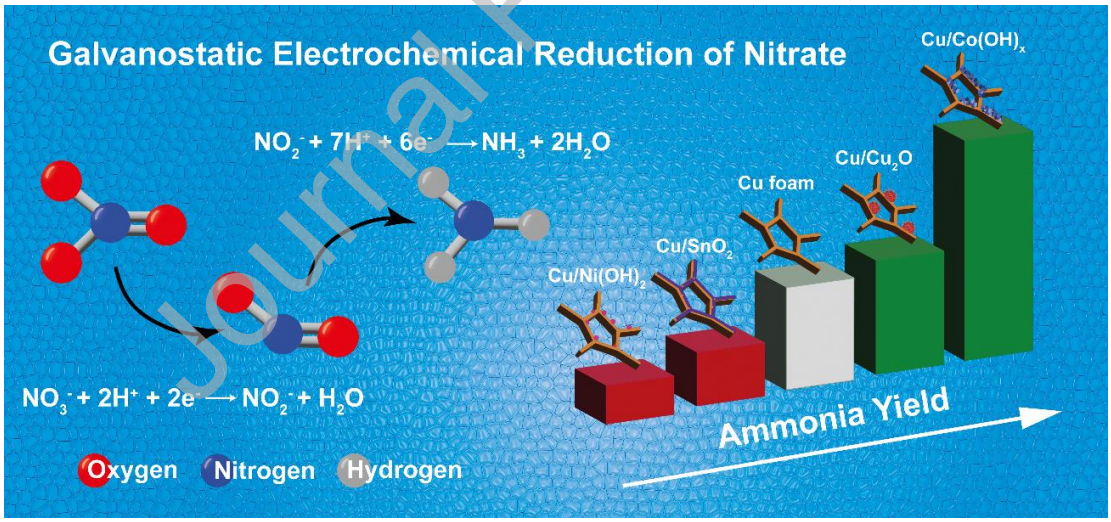


### Conflict of interest

Authors declare no conflict of interest.